Supplementary Information: Photocurrent-driven transient symmetry breaking in the Weyl semimetal TaAs

N. Sirica, P. P. Orth, M. S. Scheurer, Y.M. Dai, M.-C. Lee, P. Padmanabhan, L.T. Mix, S. W. Teitelbaum, M. Trigo, L.X. Zhao, G.F. Chen, B. Xu, R. Yang, B. Shen, C. Hu, C.-C. Lee, H. Lin, T.A. Cochran, S.A. Trugman, J.-X. Zhu, M.Z. Hasan, N. Ni, X.G. Qiu, A.J. Taylor, D.A. Yarotski, and R.P. Prasankumar

I. ISOLATED PHOTOINDUCED CHANGE IN THE SHG PATTERN

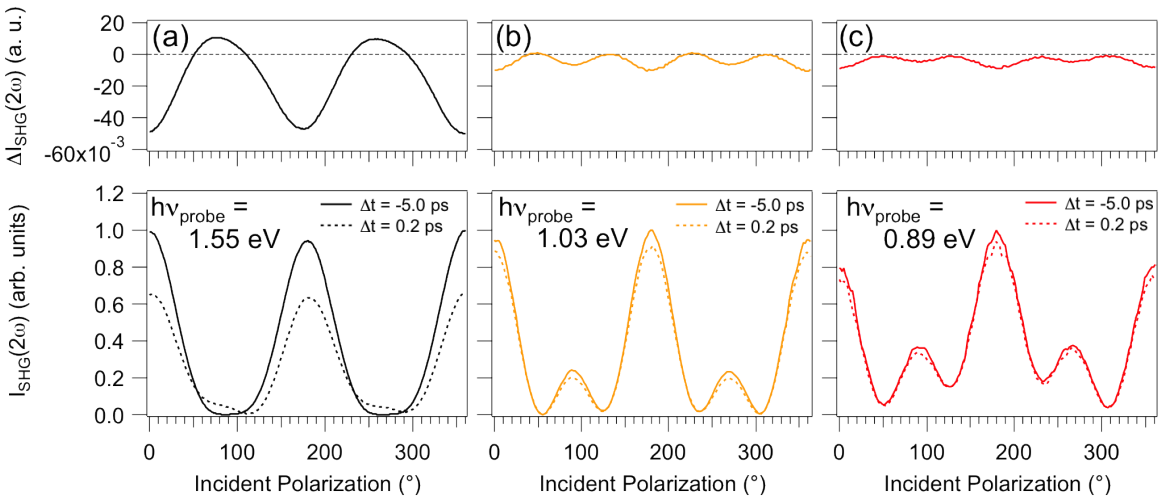

FIG. S1: Photoinduced change measured across the entire [1,1,$\bar{1}$] SHG pattern at a fixed time delay (0.2 ps). Here, photoinduced changes are isolated through taking the difference between pre- and post-pump SHG patterns generated from (a) $\hbar\omega = 1.55$ eV, (b) $\hbar\omega = 1.03$ eV and (c) $\hbar\omega = 0.89$ eV probe energies.

II. TIME-RESOLVED SHG TRACES WITH IR PROBES

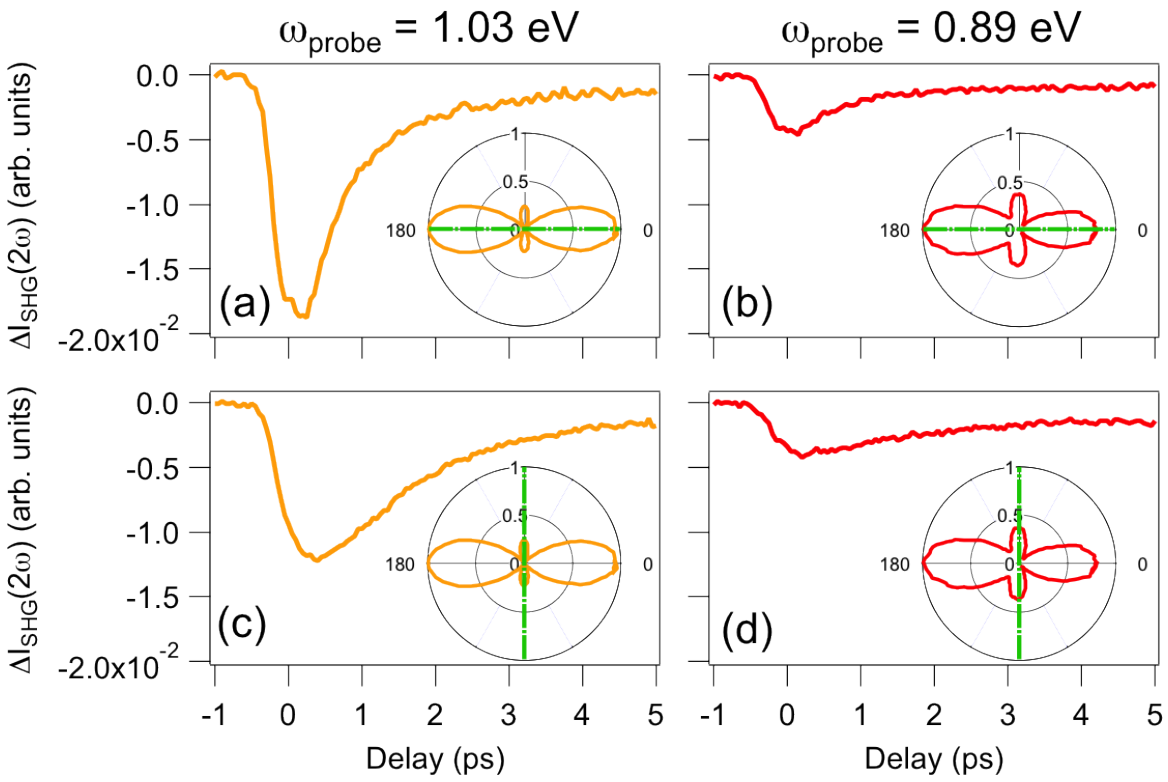

FIG. S2: Time-dependent traces of $\Delta I_{\mathrm{SHG}}(2\omega)$ measured for (a,c) 1.03 eV and (b,d) 0.89 eV probe energies following a 1.55 eV pump excitation (fluence = 4.34 mJ/cm^2). Traces reveal a suppression of both the (a,b) main lobe (0°) and (c,d) the minor lobe (90°) for the [1,1,$\bar{1}$] SHG patterns shown as insets.

III. TIME-RESOLVED X-RAY DIFFRACTION

Time-resolved X-ray diffraction (TR-XRD) experiments were performed on a TaAs single crystal having a surface normal along the (112) direction. This experiment was carried out on the X-ray pump-probe (XPP) instrument [1] at the Linac Coherent Light Source (LCLS) [2]. Optical excitation from an amplified Ti:Sapphire (1.55 eV) laser system operating at a 120 Hz repetition rate was chosen to closely match the experimental conditions used in our TR-SHG study. Lattice dynamics probed by a 35 fs, monochromatic X-ray pulse centered at 9.52 keV were measured following photoexcitation by an optical pump pulse having an excitation fluence of 2.86 mJ/cm^2. Experiments were performed in a reflection geometry, with the X-ray probe having a grazing angle of 0.5° with respect to the (112) face, and chosen to closely match the penetration depth of a normally incident optical pump pulse. Shot-to-shot fluctuations in the time delay between the optical pump and X-ray probe were

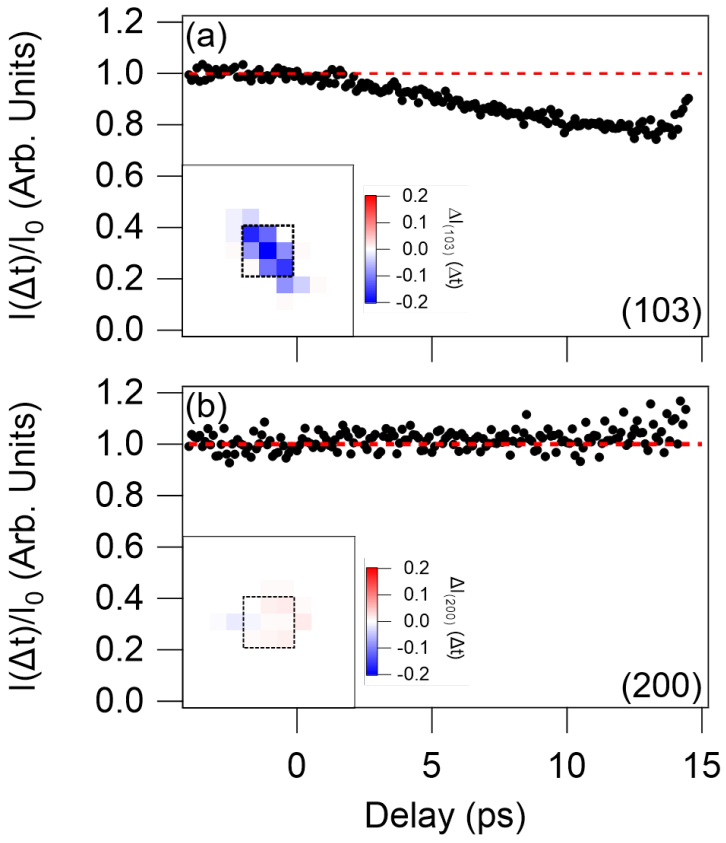

FIG. S3: Lattice dynamics of the (a) (103) and (b) (200) Bragg reflections, as integrated over the 3×3 pixel area ($\sim 4.0 \times 10^{-2}$ °/pixel) shown in the inset.

corrected for by a time diagnostic tool [3], leading to a temporal resolution better than 80 fs.

Lattice dynamics of the (103) and (200) Bragg reflections, allowed by the tetragonal symmetry of TaAs, are shown in Fig. S3. Here, a 20% attenuation of the (103) Bragg peak following 1.55 eV pump excitation occurs over a $\sim$ 10 ps timescale, consistent with lattice heating captured by the Debye-Waller effect. No such attenuation is observed for the (200) Bragg reflection, due to a dependence of the Debye-Waller factor on the scattering vector, $\vec{q}$ [4]. The insets in Fig. S3(a-b) depict a change in intensity of the (103) and (200) Bragg reflections, as defined by $\Delta I = I(\Delta t = 10 \text{ ps}) - I(\Delta t = -2 \text{ ps})$, revealing that the position and structure factor of these Bragg peaks remains constant over short timescales, suggesting the lattice plays a secondary role. In conjunction with the fact that SHG patterns measured with probe energies different from the 1.55 eV excitation energy retain $4mm1$' symmetry, these TR-XRD findings further emphasize that structural dynamics cannot underlie the symmetry breaking observed in the SHG pattern when resonantly probing the transiently excited state.

IV. PUMP HELICITY-DEPENDENCE OF PHOTOINDUCED SHG PATTERN

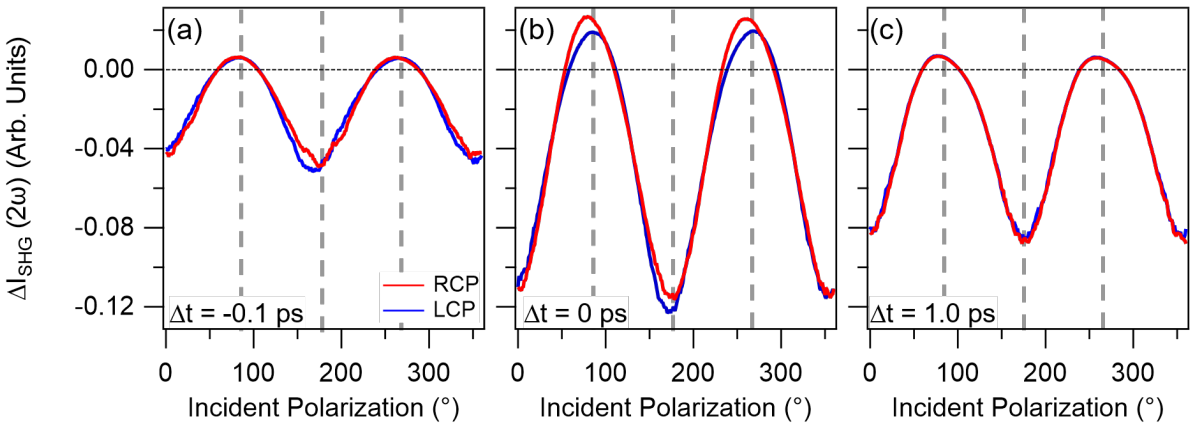

FIG. S4: Photoinduced changes to the [1,1,$\bar{1}$] SHG pattern at 1.55 eV measured as a function of pump helicity (right circularly polarized (RCP) vs. left circularly polarized (LCP)) and delay. Dashed lines at 90°, 180°, and 270° reveal a helicity dependence in the emergent asymmetric lobes as well as in the rotation of the pattern over an ultrashort (a) -0.1 ps and (b) 0 ps timescale, which is lost following a (c) 1.0 ps pump delay.

V. FLUENCE DEPENDENCE

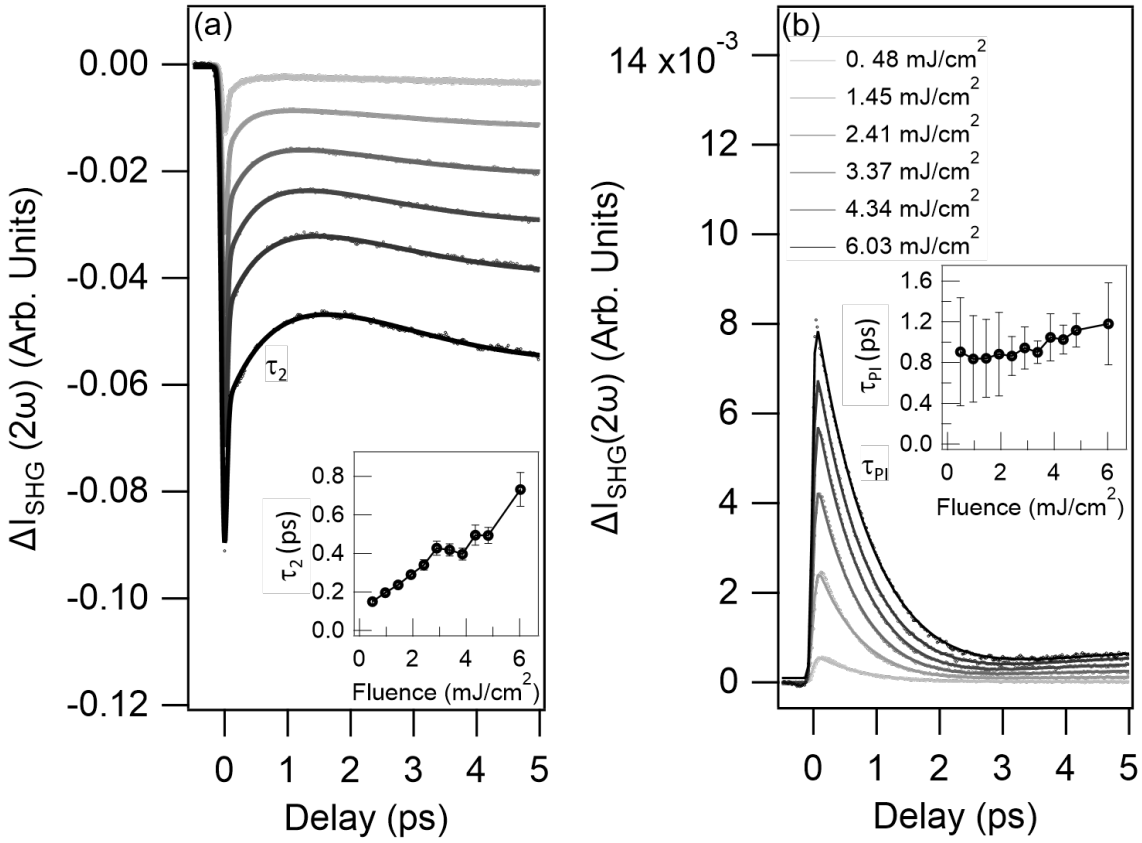

FIG. S5: Room temperature, pump fluence dependence of the time-resolved SHG traces at 1.55 eV for (a) the main lobe (0°) and (b) the asymmetric, photoinduced lobe (90°) present in the [1,1,$\bar{1}$] SHG pattern. The inset shows the fluence dependence of the relaxation times τ_2 and τ_{PI}, as determined from fits following linearly polarized pump excitation.

VI. TEMPERATURE DEPENDENCE

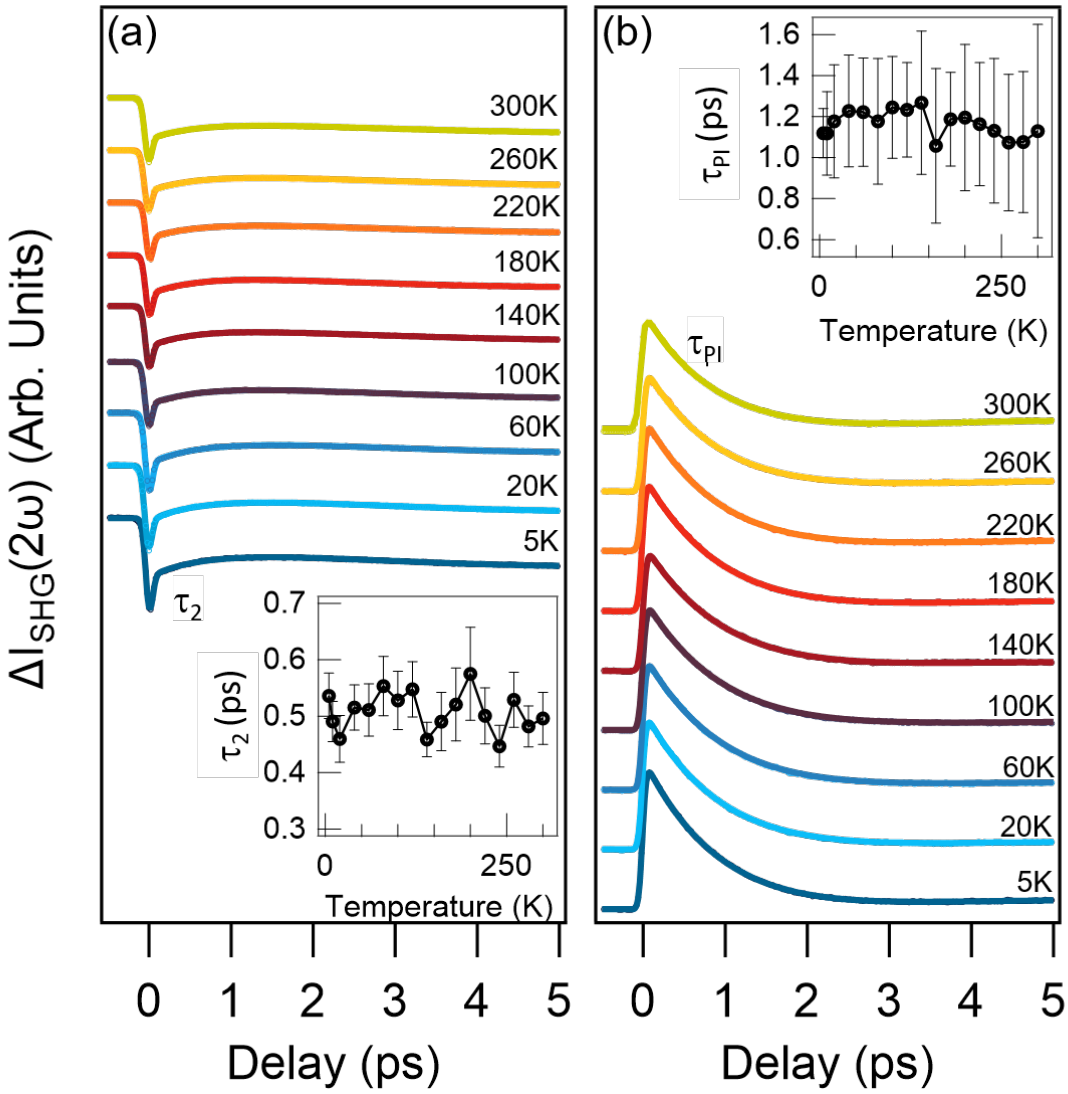

FIG. S6: Temperature dependence of the time-resolved SHG traces at 1.55 eV for (a) the main lobe (0°) and (b) the asymmetric, photoinduced lobe (90°) present in the [1,1,$\bar{1}$] SHG pattern. The inset shows the temperature dependence of the relaxation time τ_2 and τ_{PI} (main text) as determined from fits following linearly polarized pump excitation with a fluence of 4.34 mJ/cm^2.

VII. PUMP INDUCED SHIFT CURRENTS IN TAAS

The shift current is defined by Sipe and Shkrebtii [5] in terms of the nonlinear conductivity tensor σ_{abc} as

$$J_a = \sum_{b,c=x,y,z} \sigma_{abc} E_b(\omega) E_c(-\omega),$$

where the electric field of the incident light pulse is given by $E(t) = E(\omega)e^{-i\omega t} + E(-\omega)e^{i\omega t}$. Based on symmetry, the 4mm1' point group of TaAs constrains σ_{abc} to yield three independent tensor elements: $\sigma_{xxz} = \sigma_{yyz} = \sigma_{xzx} = \sigma_{yzy}$, $\sigma_{zxx} = \sigma_{zyy}$, and σ_{zzz}. For light incident on the surface normal of the (112) face, the electric field can be expressed in terms of the in-plane [1,1,$\bar{1}$] and [1,$\bar{1}$,0] axes as

$$\begin{aligned} E_x &= \frac{a}{|a_1'|} E_{[1,1,\bar{1}]} + \frac{a}{|a_2'|} E_{[1,\bar{1},0]} \\ E_y &= \frac{a}{|a_1'|} E_{[1,1,\bar{1}]} - \frac{a}{|a_2'|} E_{[1,\bar{1},0]} \\ E_z &= -\frac{c}{|a_1'|} E_{[1,1,\bar{1}]}, \end{aligned}$$

where $|a_1'| = \sqrt{2}a\sqrt{1 + \frac{c^2}{2a^2}}$ and $|a_2'| = \sqrt{2}a$ define normalization constants in terms of the lattice parameters a and c. Hence, the excitation of a shift current along the [1,$\bar{1}$,0] axis is allowed by symmetry under the condition

$$\begin{aligned} J_{[1,\bar{1},0]} &= \frac{a}{|a_2'|}(J_x - J_y) \\ &= \frac{a}{|a_2'|}(\sigma_{xxz} E_x(\omega) E_z(-\omega) + \sigma_{xzx} E_z(\omega) E_x(-\omega) - \sigma_{yyz} E_y(\omega) E_z(-\omega) - \sigma_{yzy} E_z(\omega) E_y(-\omega)) \\ &= -\frac{1}{\sqrt{1 + 2(\frac{a}{c})^2}} \sigma_{xxz} (E_{[1,1,\bar{1}]}(\omega) E_{[1,\bar{1},0]}(-\omega) + E_{[1,1,\bar{1}]}(-\omega) E_{[1,\bar{1},0]}(\omega)), \end{aligned}$$

while shift current generation along [1,1,$\bar{1}$] follows from

$$\begin{aligned} J_{[1,1,\bar{1}]} &= \frac{1}{|a_1'|}(aJ_x + aJ_y - cJ_z) \\ &= -\frac{1}{(2a^2 + c^2)\sqrt{1 + 2(\frac{a}{c})^2}} ((4a_{xxz}^2 + 2a^2\sigma_{zxx} + c^2\sigma_{zzz}) E_{[1,1,\bar{1}]}(\omega) E_{[1,1,\bar{1}]}(-\omega) + \\ &\qquad (2a^2 + c^2)\sigma_{zxx} E_{[1,\bar{1},0]}(\omega) E_{[1,\bar{1},0]}(-\omega)). \end{aligned}$$

Thus, shift current generation along [1,1,$\bar{1}$] will always be allowed by symmetry on the (112) face, regardless of polarization. In contrast, the excitation of a shift current along

[1,$\bar{1}$,0] requires the polarization to be detuned from either the [1,1,$\bar{1}$] or [1,$\bar{1}$,0] axes, with the strongest contribution coming from an equal projection along these two orthogonal axes (i.e. 45°). Such a result is similar to the symmetry constraints imposed on injection photocurrents, which are restricted to flow along the [1,$\bar{1}$,0] axis only [6].

VIII. SYMMETRY ANALYSIS OF TIME-RESOLVED SECOND-HARMONIC GENERATION PATTERNS

In this section, we describe our procedure for fitting the SHG patterns obtained before and after pump excitation ($\Delta t = \{-5.0, 0.0, 1.0, 5.0\}$ ps). In Sec. VIII A, we give details about the experimental setup. Then, in Sec. VIII B, we derive the form of the SHG electric dipole tensor for the relevant magnetic point groups (MPGs), state the general form of the expressions for the outgoing intensities in the $[1\bar{1}0]$ and $[11\bar{1}]$ channels, and describe details of our fits.

A. Experimental setup

The experimental geometry is depicted schematically in Fig. S7. It shows the scattering of an SHG probe beam relative to the normal of the (112) surface, defined as $\boldsymbol{a}_3' = \boldsymbol{a}_1 + \boldsymbol{a}_2 + 2\frac{a^2}{c^2}\boldsymbol{a}_3 \equiv [112\frac{a^2}{c^2}]$. The two high-symmetry directions on the (112) surface plane are defined as $\boldsymbol{a}_1' = \boldsymbol{a}_1 + \boldsymbol{a}_2 - \boldsymbol{a}_3 = [11\bar{1}]$ and $\boldsymbol{a}_2' = \boldsymbol{a}_1 - \boldsymbol{a}_2 = [1\bar{1}0]$. Here, we denote the conventional tetragonal basis vectors as $\boldsymbol{a}_1 \equiv [100]$, $\boldsymbol{a}_2 \equiv [010]$ and $\boldsymbol{a}_3 = [001]$, where $|\boldsymbol{a}_1| = |\boldsymbol{a}_2| = a = 3.4348$ Å and $|\boldsymbol{a}_3| = c = 11.641$ Å. We note that the vector $\boldsymbol{a}_2'$ is orthogonal to the polar axis, [001]. A transformation from the primed basis vectors to the conventional tetragonal basis vectors is obtained via $\boldsymbol{a}_\alpha' = \sum_\beta U_{\beta\alpha}\boldsymbol{a}_\beta$ with the transformation matrix

$$(U_{\beta\alpha}) = \begin{pmatrix} 1 & 1 & 1 \\ 1 & -1 & 1 \\ -1 & 0 & 2a^2/c^2 \end{pmatrix}. \tag{S1}$$

While the primed lattice vectors $\boldsymbol{a}_\alpha'$ are orthogonal $\boldsymbol{a}_\alpha' \cdot \boldsymbol{a}_\beta' \propto \delta_{\alpha\beta}$, they are not normalized. The length of the primed basis vectors is $|\boldsymbol{a}_1'| = \sqrt{2}a\sqrt{1+\frac{c^2}{2a^2}}$, $|\boldsymbol{a}_2'| = \sqrt{2}a$, and $|\boldsymbol{a}_3'| = \sqrt{2}a\sqrt{1+2\frac{a^2}{c^2}}$. It is convenient to introduce normalized basis vectors via $\boldsymbol{e}_\alpha = \boldsymbol{a}_\alpha/|\boldsymbol{a}_\alpha|$ and $\boldsymbol{e}_\alpha' = \boldsymbol{a}_\alpha'/|\boldsymbol{a}_\alpha'|$. The basis transformation matrix between these two orthonormal basis sets is achieved via $\boldsymbol{e}_\alpha' = \sum_\beta \tilde{U}_{\beta\alpha}\boldsymbol{e}_\beta$ with transformation matrix

$$(\tilde{U}_{\beta\alpha}) = \begin{pmatrix} a/|\boldsymbol{a}_1'| & a/|\boldsymbol{a}_2'| & a/|\boldsymbol{a}_3'| \\ a/|\boldsymbol{a}_1'| & -a/|\boldsymbol{a}_2'| & a/|\boldsymbol{a}_3'| \\ -c/|\boldsymbol{a}_1'| & 0 & 2a^2/(c|\boldsymbol{a}_3'|) \end{pmatrix}. \tag{S2}$$

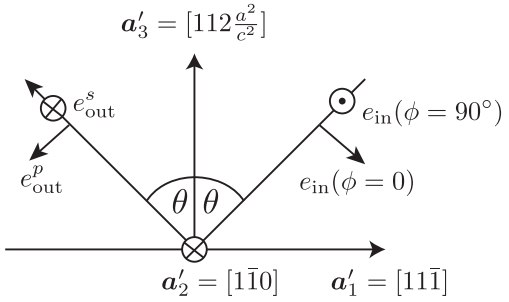

FIG. S7: Sketch of the experimental setup in which the incoming probe beam makes an angle, θ, with respect to the surface normal $\boldsymbol{a}'_3 = [112\frac{a^2}{c^2}]$ and the in-plane $\boldsymbol{a}'_1 = [11\bar{1}]$ direction. The polarization of the probe beam is continuously rotated over a full 360°, starting from $\phi = 0°$ (p-polarization) parallel to the $\boldsymbol{a}'_1$-$\boldsymbol{a}'_3$ plane.

Expressed in this orthonormal basis, the components of a vector transform according to $\boldsymbol{v} = \sum_\alpha v'_\alpha \boldsymbol{e}'_\alpha = \sum_\beta \Big(\sum_\alpha \tilde{U}_{\beta\alpha} v'_\alpha\Big)\boldsymbol{e}_\beta = \sum_\beta v_\beta \boldsymbol{e}_\beta$, leading to $v_\beta = \sum_\alpha \tilde{U}_{\beta\alpha} v'_\alpha$.

A $\tau_{\rm pump} = 80$ fs pump pulse centered at a wavelength $\lambda = 800$ nm is directed along the normal $\boldsymbol{a}'_3 = [112\frac{a^2}{c^2}]$ axis of the crystal surface. The pump pulse is linearly polarized along $\hat{e}_{\rm pump} = \boldsymbol{e}'_1 (\propto [11\bar{1}])$, up to about a 2° alignment error. The incoming probe beam has a variable wavelength between $\lambda = 800$ nm and $\lambda = 1400$ nm, making an angle of $\theta = 6°$ with respect to the surface normal $\boldsymbol{a}'_3 = [112\frac{a^2}{c^2}]$. The scattering plane of the probe beam is defined by the $\boldsymbol{e}'_1$-$\boldsymbol{e}'_3$ plane as given by the incoming and outgoing wavevectors

$$\boldsymbol{k}_{\rm in/out} = \frac{2\pi}{\lambda}\Big(-\sin\theta\, \boldsymbol{e}'_1 \mp \cos\theta\, \boldsymbol{e}'_3\Big)\,, \tag{S3}$$

where the upper sign refers to $\boldsymbol{k}_{\rm in}$. In the experiment, the incoming polarization, $\hat{\boldsymbol{e}}_{\rm in}(\phi)$, is continuously rotated, and in the primed coordinate system takes the form

$$\hat{\boldsymbol{e}}_{\rm in}(\phi) = R(\phi, \hat{\boldsymbol{k}}_{\rm in})(\cos\theta, 0, -\sin\theta)^T\,. \tag{S4}$$

Here, the rotation matrix $R(\phi, \hat{\boldsymbol{k}}_{\rm in})$ describes a rotation by angle ϕ around the direction $\hat{\boldsymbol{k}}_{\rm in} = \boldsymbol{k}_{\rm in}/|\boldsymbol{k}_{\rm in}|$. Explicitly, $\hat{\boldsymbol{e}}_{\rm in}(\phi = 0°) = \cos\theta \boldsymbol{e}'_1 - \sin\theta \boldsymbol{e}'_3$ corresponds to p-polarization and $\hat{\boldsymbol{e}}_{\rm in}(\phi = 90°) = -\boldsymbol{e}'_2$ corresponds to s-polarization.

As shown in Fig. S7, we record the outgoing SHG intensities in two channels: one parallel to $\boldsymbol{a}'_2 = [1\bar{1}0]$ (s-out) and one primarily parallel to $\boldsymbol{a}'_1 = [11\bar{1}]$ (p-out):

$$I^{[1\bar{1}0]}_{\rm SHG}(2\omega;\phi) \propto |\boldsymbol{P}(2\omega;\phi)\cdot\boldsymbol{e}'_2|^2 \tag{S5}$$

$$I^{[11\bar{1}]}_{\rm SHG}(2\omega;\phi) \propto |\boldsymbol{P}(2\omega;\phi)\cdot\boldsymbol{e}'_1|^2\,. \tag{S6}$$

Here, $\boldsymbol{P}(2\omega;\phi)$ is the nonlinear SHG polarization that is induced in the material at twice the frequency of the incoming light $\omega = 2\pi c/\lambda$. Since TaAs is non-centrosymmetric, i.e., it lacks inversion symmetry, the polarization is dominated by the bulk electric dipole response

$$\boldsymbol{P}_i(2\omega;\phi) = \sum_{j,k=x,y,z} \chi^{\mathrm{ED}}_{ijk}(2\omega;\omega,\omega)\boldsymbol{E}_j(\omega;\phi)\boldsymbol{E}_k(\omega;\phi)\,, \tag{S7}$$

where the incoming electric field is given by $\boldsymbol{E}(\omega;\phi) = E(\omega)\hat{\boldsymbol{e}}_{\mathrm{in}}(\phi)$, and the indices $i,j,k \in \{x,y,z\}$ refer to the conventional tetragonal basis directions $\boldsymbol{a}_1$, $\boldsymbol{a}_2$, $\boldsymbol{a}_3$.

B. SHG electric dipole response tensor for relevant magnetic point groups

In general, the non-linear electric dipole susceptibility χ^{ED}_{ijk} has 18 independent complex elements due to permutation symmetry in the last two indices (see Eq. (S7)):

$$\chi^{\mathrm{ED}}_{ijk} \equiv \chi_{ijk} = \left(\begin{pmatrix} xxx & xxy & xxz \\ xxy & xyy & xyz \\ xxz & xyz & xzz \end{pmatrix} \begin{pmatrix} yxx & yxy & yxz \\ yxy & yyy & yyz \\ yxz & yyz & yzz \end{pmatrix} \begin{pmatrix} zxx & zxy & zxz \\ zxy & zyy & zyz \\ zxz & zyz & zzz \end{pmatrix} \right)\,, \tag{S8}$$

where we will drop the superscript "ED"for the remainder of this discussion. The presence of magnetic point symmetries in the crystal puts constraints on the form of the tensor, according to Neumann's principle. Under a transformation with an element R of the point group, represented by a matrix R_{ij}, one finds

$$\chi_{ijk} \xrightarrow{R} \tilde{\chi}_{ijk} = \sum_{i',j',k'} R_{ii'}R_{jj'}R_{kk'}\chi_{i'j'k'} \tag{S9}$$

where $\tilde{\chi}_{ijk} = \chi_{ijk}$ by symmetry. Under time-reversal $\mathcal{T}$, which acts as complex conjugation K, the tensor transforms as $\chi_{ijk} \xrightarrow{\mathcal{T}} \tilde{\chi}_{ijk} = \chi^*_{ijk}$. In the presence of time-reversal symmetry, all elements of χ_{ijk} are thus real. For an element of the MPG that combines a spatial symmetry with time-reversal $R' = R\mathcal{T}$, one finds the constraint $\chi_{ijk} \xrightarrow{R'=\mathcal{T}R} \tilde{\chi}_{ijk} = \sum_{i',j',k'} R_{ii'}R_{jj'}R_{kk'}\chi^*_{i'j'k'} = \chi_{ijk}$.

1. *4mm1' symmetry before and long after pump excitation*

TaAs is characterized by the crystalline point group $C_{4v} = 4mm$ and possesses time-reversal symmetry in the absence of any photocurrent. The relevant MPG before and long

(> 2.0 ps) after the pump pulse is therefore $4mm1'$. The point group $4mm$ consists of a fourfold rotation $4_{0,0,z}$ around the polar $\boldsymbol{a}_3 = [001]$ axis and four vertical mirror planes that contain the polar axis. Two mirror planes are along the tetragonal coordinate axes $m_{x,0,z}$ and $m_{0,y,z}$ and two are along the diagonals $m_{x,x,z}$ and $m_{x,-x,z}$. Note that x, y, z refer to $\boldsymbol{a}_1 = [100]$, $\boldsymbol{a}_2 = [010]$ and $\boldsymbol{a}_3 = [001]$. It is thus convenient to work in the unprimed (crystal) basis and express the electric field $\boldsymbol{E}(\omega)$ in Eq. (S7) in this basis using the transformation matrix (S2).

For $4mm1'$ symmetry, the nonlinear susceptibility contains only three independent real elements, and we can use $\{xxz, zxx, zzz\} \in \mathbb{R}$ to parameterize it. Fourfold rotation symmetry, for example, which is expressed by the matrix $R[4^+_{0,0,z}] = \left(\begin{smallmatrix} 0 & -1 & 0 \\ 1 & 0 & 0 \\ 0 & 0 & 1 \end{smallmatrix}\right)$ and $R[4^-_{0,0,z}] = \left(\begin{smallmatrix} 0 & 1 & 0 \\ -1 & 0 & 0 \\ 0 & 0 & 1 \end{smallmatrix}\right)$, reduces the number of independent elements to four: $\{xxz, xyz, zxx, zzz\}$. The presence of mirror symmetries such as $R[m_{x,0,z}] = \left(\begin{smallmatrix} 1 & 0 & 0 \\ 0 & -1 & 0 \\ 0 & 0 & 1 \end{smallmatrix}\right)$ enforces $xyz \to 0$, resulting in the form of the nonlinear electric-dipole susceptibility for $4mm$ symmetry to be

$$\chi^{(C_{4v})}_{ijk} = \left(\begin{pmatrix} 0 & 0 & xxz \\ 0 & 0 & 0 \\ xxz & 0 & 0 \end{pmatrix} \begin{pmatrix} 0 & 0 & 0 \\ 0 & 0 & xxz \\ 0 & xxz & 0 \end{pmatrix} \begin{pmatrix} zxx & 0 & 0 \\ 0 & zxx & 0 \\ 0 & 0 & zzz \end{pmatrix} \right) . \tag{S10}$$

The tensor elements are real if the system is time-reversal symmetric ($4mm1'$) and complex if time-reversal is broken ($4mm$). The outgoing intensities in the two channels we measure read

$$I^{[1\bar{1}0]}_{\mathrm{SHG}} = a_1 \sin^2(2\phi) \tag{S11}$$

$$I^{[11\bar{1}]}_{\mathrm{SHG}} = \left[b_1 + b_2 \cos^2(\phi)\right]^2 . \tag{S12}$$

For a fixed incoming angle θ, the coefficient $a_1(xxz)$ is a function of xxz only and $b_1(zxx)$ will depend on zxx only. The coefficient $b_2(xxz, zxx, zzz)$ depends on all three tensor elements. Note that an (unknown) global proportionality factor has been absorbed into this definition for the matrix elements. As a result, fitting our experimental data, which is given in arbitrary units, only yields the ratios of tensor elements, but not their absolute values.

The outgoing intensities for the relevant MPG symmetries are collected in Table S1. In addition to 4mm1' symmetry, which is relevant for the bulk, static pattern, as well as for long (> 2.0 ps) pump delays, we also include the form of the outgoing intensities for m1' symmetry with diagonal mirror $m_{x,x,z}$. This is the MPG of the (112) surface, which has only one mirror plane in addition to time-reversal. Interestingly, we find that the general form of

the outgoing intensities is identical to the case of 4mm1' symmetry, which is likewise found to be valid in the absence of time-reversal. Adding the intensity of an additional electric-dipole surface response therefore does not allow for the overall rotation and photoinduced asymmetric lobes in the transiently excited $I_{\mathrm{SHG}}^{[11\bar{1}]}$ pattern to be fit.

The ratio of the fit parameters resulting from the best fits at $\Delta t = \mp 5.0$ ps in Table S2 show agreement with previous studies [7], where the zzz element is similarly found to be larger than the other two. The table also includes R^2 values of our fits from either the $[1\bar{1}0]$ or $[11\bar{1}]$ output channels. We find $R^2_{[1\bar{1}0]} = 0.97$ and $R^2_{[11\bar{1}]} = 0.99$, demonstrating that the fit accurately captures our experimental data.

MPG	Form of $I_{\mathrm{SHG}}^{[1\bar{1}0]}$	Form of $I_{\mathrm{SHG}}^{[11\bar{1}]}$
4mm1'	$a_1 s_{2\phi}^2$	$\left(b_1 + b_2 c_\phi^2\right)^2$
4mm	$a_1 s_{2\phi}^2$	$b_1 c_\phi^4 + b_2 s_\phi^4 + b_3 s_{2\phi}^2$
m1' ($m_{x,x,z}$)	$a_1 s_{2\phi}^2$	$\left(b_1 + b_2 c_\phi^2\right)^2$
m ($m_{x,x,z}$)	$a_1 s_{2\phi}^2$	$b_1 c_\phi^4 + b_2 s_\phi^4 + b_3 s_{2\phi}^2$
1'	$\left(a_1 + a_2 c_\phi^2 + a_3 s_{2\phi}\right)^2$	$\left(b_1 + b_2 c_\phi^2 + b_3 s_{2\phi}\right)^2$
1	$a_1 c_\phi^4 + a_2 c_\phi^3 s_\phi + a_3 c_\phi s_\phi^3 + a_4 s_\phi^4 + a_5 s_{2\phi}^2$	$b_1 c_\phi^4 + b_2 c_\phi^3 s_\phi + b_3 c_\phi s_\phi^3 + b_4 s_\phi^4 + b_5 s_{2\phi}^2$

TABLE S1: General form of the outgoing intensities along $[1\bar{1}0]$ (s-out) and $[11\bar{1}]$ (p-out) for the different MPG symmetries occurring in our experiment. Here, $c_\phi \equiv \cos\phi$, $s_\phi \equiv \sin\phi$ and the coefficients a_i and b_i are real. Before and long after ($\Delta t = \mp 5$ ps) pump excitation, the system has $4mm1'$ symmetry. In the presence of a pump-induced photocurrent, all spatial symmetries and time-reversal symmetry are lost, leaving the system in a reduced 1 symmetry state. We note that in the main text, we use the following notation for 1 symmetry: $I_{\mathrm{SHG}}^{[11\bar{1}]} = \sum_{n=0}^{4} \mathcal{C}_n^{[11\bar{1}]} \sin^n(\phi) \cos^{4-n}(\phi)$, corresponding to $\mathcal{C}_0^{[11\bar{1}]} = b_1$, $\mathcal{C}_1^{[11\bar{1}]} = b_2$, $\mathcal{C}_2^{[11\bar{1}]} = 2b_5$, $\mathcal{C}_3^{[11\bar{1}]} = b_3$, and $\mathcal{C}_4^{[11\bar{1}]} = b_4$. Since the symmetry of the (112) surface is given by $m1'$, where the diagonal mirror $m_{x,x,z}$ is preserved, we also include the form of the outgoing intensities for the $m1'$ point group. Because the form of the expression for $4mm1'$ and $m1'$ with diagonal mirror $m_{x,x,z}$ are identical, we conclude that the overall rotation and asymmetric lobes present at $\phi = 90°$ and $\phi = 270°$ in the photoinduced $[11\bar{1}]$ pattern, cannot be reproduced by considering an incoherent surface contribution.

4mm1'	$\Delta t = -5.0$ ps	$\Delta t = 5.0$ ps
zxx/xxz	0.12	-0.099
zzz/xxz	7.4	5.4
$b_1/\sqrt{a_1}$	0.11	-0.091
$b_2/\sqrt{a_1}$	6.4	4.9
$R^2([1\bar{1}0])$	0.97	0.97
$R^2([11\bar{1}])$	0.99	0.99

TABLE S2: Values of fit parameters and corresponding R^2 values for the best fits at $\Delta t = \mp 5.0$ ps for a 4mm1' symmetric tensor χ_{ijk}. The fits are shown in Fig. 1 of the main text in panels (a,e) and (d,f). We observe that the zzz element dominates as expected.

2. 1 symmetry in the transiently excited state

A linearly polarized pump pulse normally incident on the surface will induce a transient photocurrent directed at $\sim 6^\circ$ relative to the $m_{x,x,z}$ mirror plane of the (112) surface [6]. This photocurrent will break all spatial symmetries along with time-reversal symmetry. The MPG in the transiently excited state is therefore 1. The photocurrent decays on the timescale of $\tau_{\mathrm{PI}} \sim 1.1$ ps after which 4mm1' symmetry is restored (see panels (d,h) in Fig. 1. and Table S2).

The non-linear electric dipole tensor for 1 symmetry is of the general form in Eq. (S8) with complex elements. The outgoing intensities $I_{\mathrm{SHG}}^{[1\bar{1}0]}$ and $I_{\mathrm{SHG}}^{[11\bar{1}]}$ are then described by polynomials in $\cos\phi$ and $\sin\phi$ given in Table S1. The coefficients a_i and b_i for $i = 1, \ldots 5$ are real and lengthy expressions of the χ_{ijk}. They can be considered as independent fit parameters, as the susceptibility contains 36 independent real elements for 1 symmetry. We have obtained fits both in terms of the ten fit parameters a_i and b_i as well as in terms of the χ_{ijk}, but we state only the values for a_i and b_i obtained from best fits in Table S3. The table also contains R^2 values, which are all found to be 0.99. The resulting fits are shown in panels (b, f) and (c, g) of Fig. 1 in the main text.

For completeness, Table S4 shows the general form of the outgoing intensities $I_{\mathrm{SHG}}^{[1\bar{1}0]}$ and $I_{\mathrm{SHG}}^{[11\bar{1}]}$ for all time-reversal invariant (i.e., grey) subgroups of 4mm1' along with the corresponding crystallographic groups, where time-reversal symmetry is broken. It is interesting

to note that as long as the diagonal mirror symmetry $m_{x,x,z}$ is present, the form of the outgoing intensities is identical to the fully symmetric case with spatial 4mm symmetry.

1	$\Delta t = 0.0$ ps	$\Delta t = 1.0$ ps
a_1/a_5	0.078	0.078
a_2/a_5	0.15	0.15
a_3/a_5	-0.031	-0.031
a_4/a_5	0.087	0.086
$\mathcal{C}_0^{[11\bar{1}]}/a_5 = b_1/a_5$	20	29
$\mathcal{C}_1^{[11\bar{1}]}/a_5 = b_2/a_5$	3.2	2.6
$\mathcal{C}_3^{[11\bar{1}]}/a_5 = b_3/a_5$	2.2	1.9
$\mathcal{C}_4^{[11\bar{1}]}/a_5 = b_4/a_5$	1.7	0.70
$\frac{1}{2}\mathcal{C}_2^{[11\bar{1}]}/a_5 = b_5/a_5$	-0.45	-0.29
$R^2([1,\bar{1},0])$	0.99	0.99
$R^2([1,1,\bar{1}])$	0.99	0.99

TABLE S3: Fit parameters and corresponding R^2 values for a 1 point group symmetry of the photoexcited state. The general form of the outgoing intensities is (see Table S1): $I_{\mathrm{SHG}}^{[1\bar{1}0]} = a_1 c_\phi^4 + a_2 c_\phi^3 s_\phi + a_3 c_\phi s_\phi^3 + a_4 s_\phi^4 + a_5 s_{2\phi}^2$ and $I_{\mathrm{SHG}}^{[11\bar{1}]} = b_1 c_\phi^4 + b_2 c_\phi^3 s_\phi + b_3 c_\phi s_\phi^3 + b_4 s_\phi^4 + b_5 s_{2\phi}^2$. We note that in the main text, we use the following notation for 1 symmetry, $I_{\mathrm{SHG}}^{[11\bar{1}]} = \sum_{n=0}^{4} \mathcal{C}_n^{[11\bar{1}]} \sin^n(\phi) \cos^{4-n}(\phi)$, corresponding to $\mathcal{C}_0^{[11\bar{1}]} = b_1$, $\mathcal{C}_1^{[11\bar{1}]} = b_2$, $\mathcal{C}_2^{[11\bar{1}]} = 2b_5$, $\mathcal{C}_3^{[11\bar{1}]} = b_3$, and $\mathcal{C}_4^{[11\bar{1}]} = b_4$. The overall rotation of the $I_{\mathrm{SHG}}^{[11\bar{1}]}$ pattern and anisotropy in the photoinduced lobes are captured by the b_2 coefficient. Asymmetry in the photoinduced lobes is given by a non-zero b_3, b_4 coefficients (predominately b_3 in our fits). The coefficient b_4 is responsible for a finite value of the local minima around $\phi = 90°, 270°$.

C. Discussion of symmetry breaking transient features in the SHG patterns

Let us briefly discuss which of the terms in the general form of the outgoing intensities allow us to capture the observed transient features in the SHG pattern. To recall, in the transient regime at $\Delta t = 0.0$ ps and $\Delta t = 1.0$ ps, we find (i) an overall rotation of the $I_{\mathrm{SHG}}^{[11\bar{1}]}$ pattern by $\sim 2.5°$, and (ii) emergent, asymmetric lobes at $\phi = 90°$ and $\phi = 270°$. In contrast

MPG	Form of $I_{\mathrm{SHG}}^{[1\bar{1}0]}$	Form of $I_{\mathrm{SHG}}^{[11\bar{1}]}$
2mm1', $(m_{x,-x,z}, m_{x,x,z})$	$a_1 s_{2\phi}^2$	$\left(b_1 + b_2 c_\phi^2\right)^2$
2mm, $(m_{x,-x,z}, m_{x,x,z})$	$a_1 s_{2\phi}^2$	$b_1 c_\phi^4 + b_2 s_\phi^4 + b_3 s_{2\phi}^2$
2mm1', $(m_{x,0,z}, m_{0,y,z})$	$\left(a_1 c_\phi^2 + a_2 s_{2\phi}\right)^2$	$\left(b_1 + b_2 c_\phi^2 + b_3 s_{2\phi}\right)^2$
2mm, $(m_{x,0,z}, m_{0,y,z})$	$c_\phi^2\left(a_1 + a_2 c_\phi^2 + a_3 s_{2\phi}\right)$	$b_1 c_\phi^4 + b_2 c_\phi^3 s_\phi + b_3 c_\phi s_\phi^3 + b_4 s_\phi^4 + b_5 s_{2\phi}^2$
41'	$\left(a_1 c_\phi^2 + a_2 s_{2\phi}\right)^2$	$\left(b_1 + b_2 c_\phi^2 + b_3 s_{2\phi}\right)^2$
4	$c_\phi^2\left(a_1 + a_2 c_\phi^2 + a_3 s_{2\phi}\right)$	$b_1 c_\phi^4 + b_2 c_\phi^3 s_\phi + b_3 c_\phi s_\phi^3 + b_4 s_\phi^4 + b_5 s_{2\phi}^2$
m1' $(m_{x,0,z})$	$\left(a_1 + a_2 c_\phi^2 + a_3 s_{2\phi}\right)^2$	$\left(b_1 + b_2 c_\phi^2 + b_3 s_{2\phi}\right)^2$
m $(m_{x,0,z})$	$a_1 c_\phi^4 + a_2 c_\phi^3 s_\phi + a_3 c_\phi s_\phi^3 + a_4 s_\phi^4 + a_5 s_{2\phi}^2$	$b_1 c_\phi^4 + b_2 c_\phi^3 s_\phi + b_3 c_\phi s_\phi^3 + b_4 s_\phi^4 + b_5 s_{2\phi}^2$
21'	$\left(a_1 c_\phi^2 + a_2 s_{2\phi}\right)^2$	$\left(b_1 + b_2 c_\phi^2 + b_3 s_{2\phi}\right)^2$
2	$c_\phi^2\left(a_1 + a_2 c_\phi^2 + a_3 s_{2\phi}\right)$	$b_1 c_\phi^4 + b_2 c_\phi^3 s_\phi + b_3 c_\phi s_\phi^3 + b_4 s_\phi^4 + b_5 s_{2\phi}^2$

TABLE S4: General form of the outgoing intensities along $[1\bar{1}0]$ (s-out) and $[11\bar{1}]$ (p-out) for the remaining white and corresponding gray MPGs that are derived from 4mm1'. Here, $c_\phi \equiv \cos\phi$, $s_\phi \equiv \sin\phi$ and the coefficients a_i and b_i are real. The expression for $m1'$ and m with mirror $m_{0,y,z}$ is identical to the one with $m_{x,0,z}$. We state these expressions for completeness, but note that we do not consider other possible black-white magnetic subgroups of 4mm1', as they are not relevant to our experiment.

the $I_{\mathrm{SHG}}^{[1\bar{1}0]}$ pattern remains unchanged under pump excitation.

Importantly, neither of the two features, (i) and (ii), described above can be captured by a tensor constrained by 4mm1' symmetry, as the lobes must remain pinned to the coordinate axes. While the emergence of small lobes at $\phi = 90°$ (and $\phi = 270°$) can be enforced by increasing the value of b_1, these will necessarily be symmetric around a maximum at $\phi = 90°$. Similarly, the overall rotation can be accounted for in the absence of time-reversal symmetry for 4mm, but the asymmetry of the photoinduced lobes at $\phi = 90°$ and $\phi = 270°$ cannot be obtained with a 4mm tensor. Since the diagonal mirror $m_{x,x,z}$ enforces the form for m1' (m) to be identical to 4mm1' (4mm) (see Table S1), the same applies for a (surface) tensor constrained by m1' (with $m_{x,x,z}$ mirror symmetry).

Interestingly, the asymmetry of the small lobes at $\phi = 90°$ and $\phi = 270°$ cannot be produced in the presence of time-reversal symmetry, even if all spatial symmetries are broken,

i.e. for 1' symmetry. This is shown most transparently by rewriting

$$(b_1 \sin^2\phi + b_2 \cos^2\phi + b_3 \sin\phi\cos\phi)^2 = \left[a_1 \cos^2(\phi-\phi_0) + a_2 \sin^2(\phi-\phi_0)\right]^2 \qquad \text{(S13)}$$

with global shift angle $\phi_0 = \frac{1}{2}\sin^{-1}[b_3/(a_1-a_2)]$ and $a_1 = \frac{b}{2} \mp \frac{\sqrt{\beta}}{2}$, $a_2 = \frac{b}{2} \pm \frac{\sqrt{\beta}}{2}$, where $b = b_1 + b_2$ and $\beta = (b_1 - b_2)^2 + b_3^2$. The sign in the expressions for a_1 and a_2 is chosen such that $\text{sign}(a_1 - a_2) = \text{sign}(b_1 - b_2)$. Note that $a_1 - a_2 = \mp\sqrt{\beta}$. While the expression for 1' can thus reproduce a global shift of the pattern by ϕ_0, the pattern is necessarily symmetric around the lobes and in particular the small side lobes close to $\pi/2$. In contrast, the observed asymmetry shown in Fig. 1 (b, f, c, g) is fully consistent with 1 symmetry. Hence, the asymmetry of these emergent lobes can be directly associated with a breaking of both time-reversal and mirror $m_{x,x,z}$ symmetry brought on by photocurrent generation.

In our fit using 1 symmetry, the overall rotation is (mostly) accounted for by the coefficient $b_2 \equiv \mathcal{C}_1^{[11\bar{1}]}$ (see Table S3). The asymmetry of the photoinduced lobes at $\phi = 90°$ and $\phi = 270°$ is (mostly) expressed by the fit parameter $b_3 \equiv \mathcal{C}_3^{[11\bar{1}]}$, because it is multiplied by $\sin^3\phi\cos\phi$ and is thus larger close to $\phi = \pi/2$ than $\sin\phi\cos^3\phi$. The magnitude of the side lobes at $\phi = \pi/2$ is encoded by the fit parameter $b_4 \equiv \mathcal{C}_4^{[11\bar{1}]}$ (which is multiplied by $\sin^4\phi$). While the largest parameter is $b_1 \equiv \mathcal{C}_0^{[11\bar{1}]}$, which is responsible for the main lobes at $\phi = 0°$, we find that at $\Delta t = 0.0(1.0)$ ps the "overall rotation parameter" $b_2/b_1 = \mathcal{C}_1^{[11\bar{1}]}/\mathcal{C}_0^{[11\bar{1}]} = 0.16(0.09)$ and "lobe asymmetry parameter" $b_3/b_1 = \mathcal{C}_3^{[11\bar{1}]}/\mathcal{C}_0^{[11\bar{1}]} = 0.11(0.07)$ are still significant. In other words, a symmetry breaking photocurrent has a significant impact of order 10 - 15% on the $I_{\text{SHG}}^{[11\bar{1}]}$ pattern.

IX. FIRST-PRINCIPLES CALCULATIONS OF OPTICAL CONDUCTIVITY IN TAAS

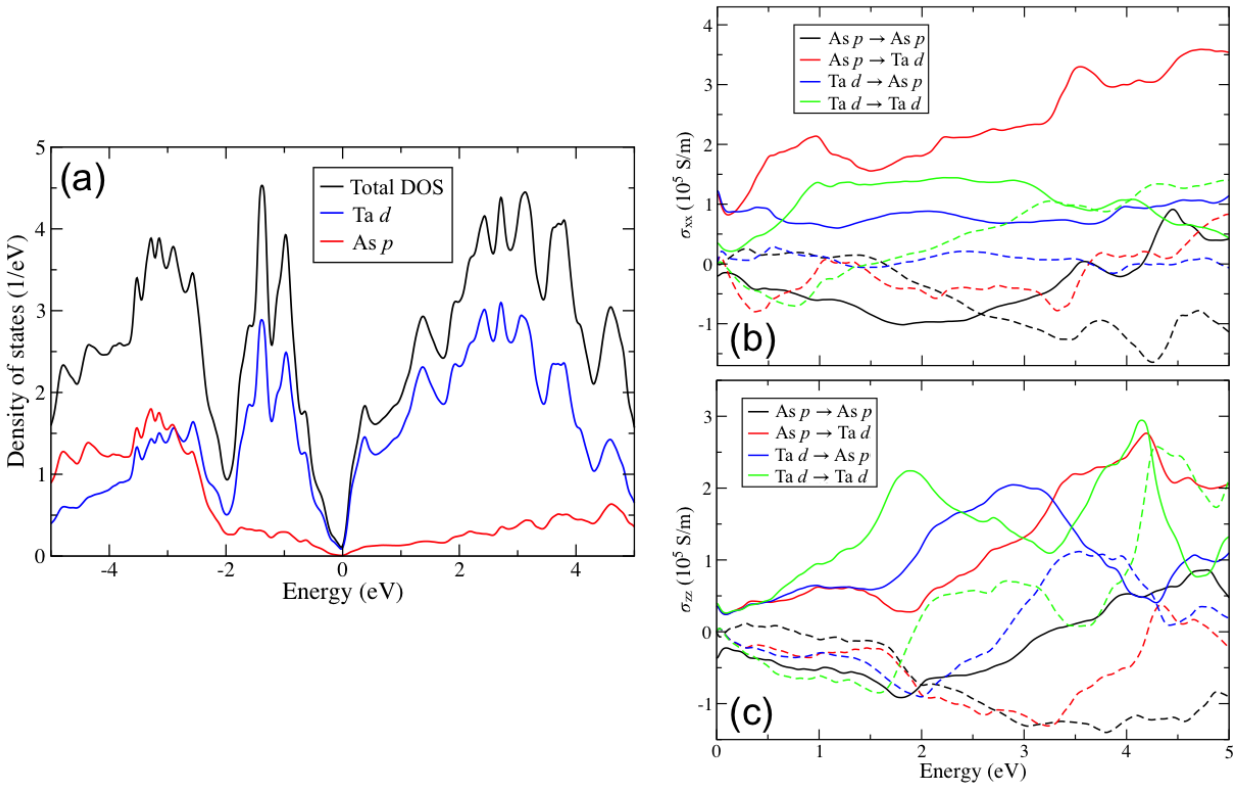

FIG. S8: (a) Total density-of-states (DOS) of TaAs (black) decomposed into Ta-d (blue) and As-p (red) orbital contributions. Calculated optical conductivity for (b) $\sigma_{xx} = \sigma_{yy}$ and (c) σ_{zz} decomposed to show different orbital contributions. Here, solid and dashed curves represent the real and imaginary parts of the optical conductivity, respectively.

The calculated density-of-states (DOS) of TaAs is shown in Fig. S8(a). The DOS near the Fermi energy (0 eV) mainly comes from the contribution of Ta-d orbitals. From the DOS, we find that the optical conductivity can be described by four contributions: the transitions from As-p to As-p orbitals, As-p to Ta-d orbitals, Ta-d to As-p orbitals, and Ta-d to Ta-d orbitals. In the Kubo-Greenwood formula, there are two momentum matrix elements in the numerator. The orbital contribution for the transitions can be defined via one of the momentum matrices through, $\langle kM|\hat{p}_{x\ \vee\ y\ \vee\ z}|kN\rangle$, where M and N denote the pseudoatomic orbitals. The orbital contribution for the optical conductivity, $\sigma(\omega)$ is shown in Fig. S8(b-c) for the σ_{xx} and σ_{zz} components, respectively. In Fig. S8(b), a prominent contribution close

to 1.0 eV in the in-plane conductivity σ_{xx} (or σ_{yy}) can be identified as the result of an As-p to Ta-d transition. In contrast, Fig. S8(c) shows a prominent contribution close to 1.9 eV for the out-of-plane conductivity σ_{zz}, which can be identified as the result of a Ta-d to Ta-d transition.

---

[1] M. Chollet, R. Alonso-Mori, M. Cammarata, D. Damiani, J. Defever, J. T. Delor, Y. Feng, J. M. Glownia, J. B. Langton, S. Nelson, et al., Journal of Synchrotron Radiation **22**, 503 (2015), URL https://doi.org/10.1107/S1600577515005135.

[2] C. Bostedt, S. Boutet, D. M. Fritz, Z. Huang, H. J. Lee, H. T. Lemke, A. Robert, W. F. Schlotter, J. J. Turner, and G. J. Williams, Rev. Mod. Phys. **88**, 015007 (2016), URL https://link.aps.org/doi/10.1103/RevModPhys.88.015007.

[3] M. Harmand, R. Coffee, M. R. Bionta, M. Chollet, D. French, D. Zhu, D. M. Fritz, H. T. Lemke, N. Medvedev, B. Ziaja, et al., Nature Photonics **7**, 215 (2013), URL https://doi.org/10.1038/nphoton.2013.11.

[4] B. Warren, *X-Ray Diffraction* (Dover Publications, New York, New York, 1990).

[5] J. E. Sipe and A. I. Shkrebtii, Phys. Rev. B **61**, 5337 (2000), URL https://link.aps.org/doi/10.1103/PhysRevB.61.5337.

[6] N. Sirica, R. I. Tobey, L. X. Zhao, G. F. Chen, B. Xu, R. Yang, B. Shen, D. A. Yarotski, P. Bowlan, S. A. Trugman, et al., Phys. Rev. Lett. **122**, 197401 (2019), URL https://link.aps.org/doi/10.1103/PhysRevLett.122.197401.

[7] S. Patankar, L. Wu, B. Lu, M. Rai, J. D. Tran, T. Morimoto, D. E. Parker, A. G. Grushin, N. L. Nair, J. G. Analytis, et al., Phys. Rev. B **98**, 165113 (2018), URL https://link.aps.org/doi/10.1103/PhysRevB.98.165113.